

Globular cluster populations and the kinematical fingerprints of minor mergers

N. C. Amorisco^{1,2*}

¹*Institute for Theory and Computation, Harvard-Smithsonian Center for Astrophysics, 60 Garden St., MS-51, Cambridge, MA 02138, USA*

²*Max Planck Institute for Astrophysics, Karl-Schwarzschild-Strasse 1, 85748 Garching, Germany*

29 October 2018

ABSTRACT

We use Monte Carlo Λ CDM assembly histories, minor-merger N-body simulations and empirical relations between halo mass and the globular cluster (GC) abundance to study the kinematical properties of halo GCs in massive galaxies, with $M_{\text{vir}}(z=0) = 10^{13.5} M_{\odot}$. While the accreted stellar halo is dominated by the contributions of massive satellites, we show that satellites with low virial mass (i.e. low satellite-to-host virial mass ratio, VMRs) are important contributors to the population of accreted GCs. The relative contribution of accretion events with low VMRs is highest for the halo population of blue GCs and gradually decreases for red GCs and accreted stars. As a consequence of the reduced efficiency of dynamical friction on minor mergers, our populations of cosmologically accreted blue GCs are systematically more spatially extended and have higher velocity dispersions than for red GCs, in agreement with observations. For the same reason, assembly histories including a higher fraction of minor mergers result in more spatially extended GC populations. GC line-of-sight velocity distributions featuring negative values of the kurtosis κ , as recently observed, are ubiquitous in our models. Therefore, $\kappa < 0$ is not at odds with an accretion scenario, and in fact a fingerprint of the important contribution of minor mergers. However, our populations of accreted GCs remain mostly radially biased, with profiles of the anisotropy parameter β that are mildly radial in the center ($\beta(r < 10 \text{ kpc}) \sim 0.2$) and strongly radially anisotropic at large galactocentric distances ($\beta(r > 30 \text{ kpc}) \gtrsim 0.6$), for both red and blue populations.

Key words: galaxies: structure — galaxies: star clusters — galaxies: kinematics and dynamics — galaxies: formation

1 INTRODUCTION

Globular clusters (GCs) are valuable tracers of the kinematics and assembly of galaxies. Compact and bright, they are observable in distant galaxies in the local universe as well as at large radii from the galaxy centre. As such, GCs have had a fundamental role in studies aimed at probing the dark matter distribution in massive early type galaxies (e.g., Grillmair et al. 1994; Saglia et al. 2000; Romanowsky & Kochanek 2001; Schuberth et al. 2012; Agnello et al. 2014; Napolitano et al. 2014; Pota et al. 2015; Zhu et al. 2016, and references therein) or at constraining their assembly history (e.g., Zepf & Ashman 1993; Forbes et al. 1997; Côté et al. 1998; Brodie & Strader 2006; Li & Gnedin 2014; Mistani et al. 2016, among many others).

Intriguingly, GC populations appear to have strong ties to dark matter haloes. It is well known that the efficiency of

the process of galaxy formation is a markedly non-monotonic function of halo mass, with a characteristic peak at around Milky Way mass haloes (e.g., Guo et al. 2010; Moster et al. 2010; Behroozi et al. 2013). In turn, the GC abundance – or the total stellar mass in GCs – appears to be roughly proportional to halo mass (e.g., Blakeslee et al. 1997; Spitler & Forbes 2009; Georgiev et al. 2010; Hudson et al. 2014; Harris et al. 2017). Such an approximately linear relation seems to extend to low-mass haloes (Forbes et al. 2018), so that, within a Λ CDM framework, it directly follows that a considerable fraction of GCs in massive galaxies have not been formed within the main progenitor, but rather they have been accumulated through hierarchical merging (e.g., White & Frenk 1991). In fact, a close to linear relation between halo mass and GC abundance works well with the scenario in which most GCs, and especially metal poor GCs, form at high redshift (e.g., Peebles 1984; Ricotti 2002; Kravtsov & Gnedin 2005; Brodie & Strader 2006, and

* E-mail: nicola.amorisco@cfa.harvard.edu

references therein), as hierarchical assembly would approximately preserve this linearity.

The kinematics of accreted stellar populations deposited in the halo of galaxies through hierarchical accretion has been studied in detail, with particular attention to the case of Milky Way (MW) mass galaxies (e.g., [Dekel et al. 2005](#); [Abadi et al. 2006](#); [Moore et al. 2006](#); [Oñorbe et al. 2007](#); [Cooper et al. 2010](#); [Wu et al. 2014](#)). A general result of these analyses is that radial orbits are dominant, and that the deposited stellar material is therefore characterized by a marked radial anisotropy, $\beta > 0$, where $\beta(r)$ is the classical anisotropy parameter

$$\beta(r) = 1 - \frac{\sigma_t^2(r)}{2\sigma_r^2(r)}, \quad (1)$$

with σ_t and σ_r being respectively the tangential and radial stellar velocity dispersions. Given the generality of this finding and the common accretion origin of halo GCs, it would seem only natural that the population of accreted GCs should share this property, and also have radially biased orbits.

The recent increase in both size and quality of GC spectroscopic datasets (e.g., [Pota et al. 2013](#); [Zhang et al. 2015](#); [Forbes et al. 2017](#)) have however sparked a question on whether the simple picture above may be incomplete. For instance, following the described line of thought, the line-of-sight velocity distribution (LOSVD) of accreted GCs should be characterised by a positive kurtosis, as generally expected for populations with orbital distributions that have a strong radial bias (e.g., [Gerhard 1993](#); [van der Marel & Franx 1993](#)). For a LOSVD $f_{LOS}(v, R)$, the kurtosis κ quantifies departures from Gaussianity that are symmetric with respect to the mean μ :

$$\kappa(R) + 3 = \frac{1}{\sigma_{LOS}^4(R)} \int dv f_{LOS}(v, R) [v - \mu(R)]^4. \quad (2)$$

Here R is the projected galactocentric radius, $\sigma_{LOS}(R)$ is the LOS velocity dispersion, and the LOSVD $f_{LOS}(v, R)$ is indeed the distribution of LOS velocities at the radius R , normalised to unity. Radially biased populations are characterised by LOSVDs with heavy tails and a sharp central peak, corresponding to $\kappa > 0$ (see e.g., [Amorisco & Evans 2012](#)). Instead, [Pota et al. \(2013\)](#) have shown that both red and blue GC populations often display LOSVDs with kurtosis $\kappa \sim 0$, suggesting orbits that are close to isotropic. Positive values of κ are often observed at large galactocentric radii, but negative values of κ are common for both red and blue GCs in the galaxy’s central regions, as also confirmed by [Zhang et al. \(2015\)](#). This is unexpected and, if taken at face value, this finding could be interpreted as a suggestion of some degree of *tangential* anisotropy. Such a conclusion would be unwarranted: it is well known that kurtosis is only a rough proxy for actual orbital structure, and that there’s no one-to-one relation between kurtosis and anisotropy (e.g., [Gerhard 1993](#); [van der Marel & Franx 1993](#); [Napolitano et al. 2014](#)). However, the finding that negative values of κ are common in GC populations remains surprising when put in comparison with the stellar halo. Generalizing from the kinematic properties of the latter, negative values of κ would appear at odds with the scenario in which a substantial fraction of all GCs are accreted.

In this paper, we show that there is in fact no contra-

dition between the observed negative values of the kurtosis in the LOSVDs of halo GCs and the scenario in which most of them have an accretion origin. We show that negative values of the kurtosis are expected within a Λ CDM framework when minor mergers are the dominant contributing channel of an accreted population, without the need to invoke additional physical processes. Due to the approximate linearity of the relation between halo mass and GC abundance, and in opposition to stellar haloes, minor mergers are indeed dominant in assembling the accreted populations of GCs, especially for blue metal poor GCs.

In Section 2 we use Λ CDM assembly histories to show how stellar and GC haloes have systematically different mean progenitors. Section 3 concentrates on the kinematical properties of material deposited in the accreted halo by satellites with different properties. Section 4 builds toy models for the populations of cosmologically accreted GCs, and focuses on their intrinsic and projected kinematic properties. Section 5 discusses results and lays out the Conclusions.

2 THE PROGENITORS OF STELLAR AND GC HALOES

We construct two sets of mock Λ CDM assembly histories, one for haloes of MW-like virial mass, $\log M_{\text{host}}(z=0)/M_{\odot} = 12.3$, and one for haloes with virial mass $\log M_{\text{host}}(z=0)/M_{\odot} = 13.5$, representative of a massive central galaxy. Each set explores 10^3 individual halo assembly histories. Individual assembly histories are composed of Monte Carlo-generated accretion events, randomly sampling from the merger rates of dark matter haloes in the Millennium simulation ([Fakhouri et al. 2010](#)), and collect all mergers experienced by the main progenitor. Statistically, these assembly histories reproduce the growth of haloes in the Millennium simulation, in terms ([Fakhouri et al. 2010](#)) of the distribution of accretion redshifts and of satellite-to-host virial mass ratios, in both mean and scatter. We keep track of all accretion events onto the main progenitor for satellites with virial mass $\log M_{\text{sat}}/M_{\odot} > 7$ at the time of accretion, since $z = 6$. These accreted satellites contribute stars to the accreted halo population of the host according to a standard stellar-to-halo mass relation (SHMR). In particular, we adopt a mean relation as presented by [Garrison-Kimmel et al. \(2014\)](#), and assume a log-normal scatter of 0.3 dex (individual values are randomly sampled from such distribution). For simplicity, both mean relation and scatter are assumed to be independent of redshift. The resulting SHMR is displayed as a black line in the left panel of Fig. 1. We recall that below the break at MW-like masses, the log-log slope of this SHMR is of ≈ 1.9 .

Accreted satellites also contribute to the accreted GC population of the host. We track red and blue GCs separately and assume that the GC population of each satellite is a function of the halo mass at accretion. In particular, we

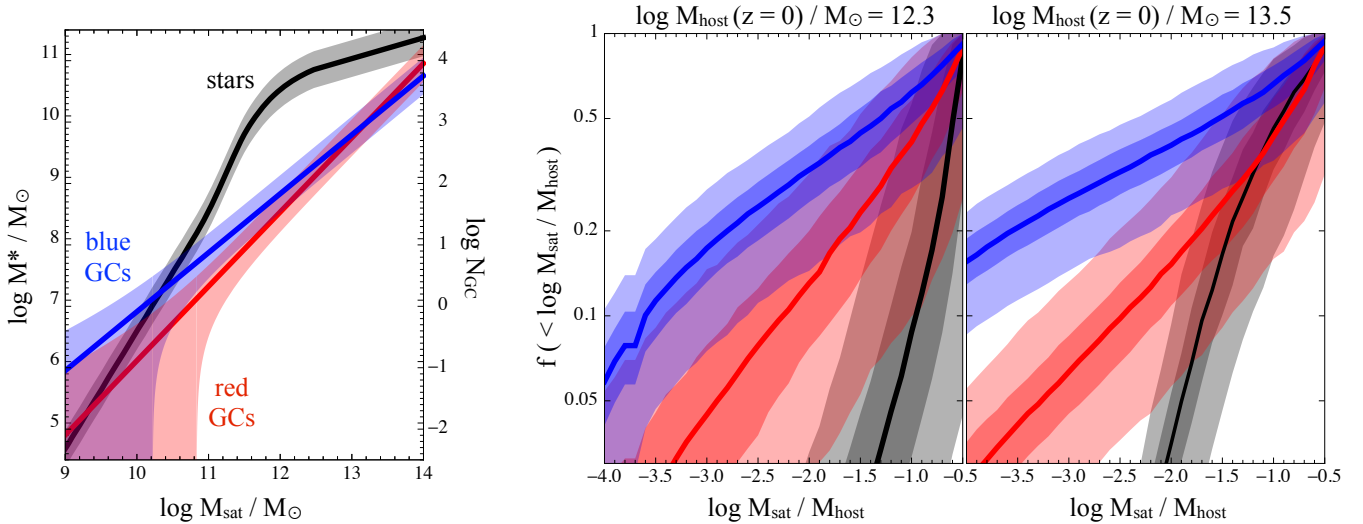


Figure 1. Left panel: the relation between halo mass of the contributing satellites and the contributed stellar mass (in black), red GCs (in red), blue GCs (in blue). The shading identifies the 1-sigma regions around the mean model relations (including both intrinsic and Poisson scatter for GCs). Middle and right panels: cumulative contributions to the accreted stellar and GC populations, as a function of the virial mass ratio at accretion, $\log M_{\text{sat}}/M_{\text{host}}$. Thick lines identify medians, shaded regions extend between the {5, 25, 75, 95}% quantiles, over a sample of 10^3 halo assembly histories. The middle panel refers to the halo of a Milky Way-like galaxy $\log M_{\text{host}}(z=0)/M_{\odot} = 12.3$. The right panel to a massive elliptical galaxy $\log M_{\text{host}}(z=0)/M_{\odot} = 13.5$.

adopt mean relations¹ as measured by Harris et al. (2015):

$$\begin{cases} \log N_{GC,red} &= 1.8 + 1.21 (\log M_{\text{sat}} - 12.2) \\ \log N_{GC,blue} &= 2.0 + 0.96 (\log M_{\text{sat}} - 12.2) \end{cases}, \quad (3)$$

where $N_{GC,red}$ and $N_{GC,blue}$ are respectively the abundance of red and blue GCs. With a log-log slope of 0.96, the abundance of Blue GCs is approximately proportional to the virial mass of the satellite M_{sat} . The abundance in red GCs is slightly steeper, for a log-log slope of 1.21. We take that, in addition to Poisson noise, the intrinsic scatter around these mean relations is of 0.3 dex. The left panel of Fig. 1 compares the prescriptions above with the SHMR; the shading shows the 1-sigma region for each relation. It is worth noticing that while the empirical relations (3) have been measured at $z=0$, we instead require estimates of the GC abundance of satellites at the time of accretion. In absence of measurements for the same relations as a function of redshift, we take that the abundances (3) are independent of redshift: satellites contribute GCs according to their halo mass at accretion. Note that this is the same simplifying assumption made for the SHMR. Though not ideal, this can be considered conservative here. With respect to a model in which GCs are formed at high redshift with an abundance that is proportional to halo mass *at the time of formation* (see e.g., Boylan-Kolchin 2017), the present model implies an underestimation of the role of minor mergers, as massive haloes assemble more recently.

Given the set of minimal hypotheses above, Figure 1

¹ We recall that these relations refer to the integrated GC population. The measured GC abundances used for their derivation are therefore based on a number of hypotheses regarding the GC luminosity function, as well as on the spatial density distribution of the GC population when the field coverage does not include the entire target galaxy. We refer the reader to Harris et al. (2013) and Jordán et al. (2007) for more details.

shows the cumulative fraction f of accreted halo populations, in stars and GCs, contributed by satellites with different satellite-to-host virial mass ratio at accretion (VMR), $\log M_{\text{sat}}/M_{\text{host}}$. The middle panel refers to our set of MW-like haloes. The right panel to our massive haloes with $M_{\text{vir}}(z=0) = 10^{13.5} M_{\odot}$. Thick lines show median relations, the shaded regions extend between the {5, 25, 75, 95}% quantiles. Fig. 1 shows very clearly that the average progenitor satellite of stellar halo and accreted GC populations are remarkably different.

2.1 MW-like haloes

As shown in the middle panel of Fig. 1, the contribution of low-mass satellites to the accreted stellar halo of MW like galaxies drops quickly at $\log M_{\text{sat}}/M_{\text{host}} \lesssim -1$. This is a well-known result (e.g., Bullock & Johnston 2005; Sales et al. 2007; Cooper et al. 2010; Deason et al. 2016; Amorisco 2017a) and a direct consequence of the steepness of the SHMR at virial masses $\log M_{\text{sat}}/M_{\odot} \lesssim 12$, with a log-log slope of ~ 1.9 (e.g., Garrison-Kimmel et al. 2014, 2017; Jethwa et al. 2018). As shown by the first panel of Fig. 1, the relations (3) prescribe GC abundances that are considerably less steep with halo mass, resulting in much higher fractions of accreted GCs being contributed by satellites with low VMR. For example, accretion events with $\log M_{\text{sat}}/M_{\text{host}} < 1/50$ contribute between 30 and 48% (respectively 25 and 75% quantiles) of the blue GCs in MW-like galaxies respectively between 10 and 27% of the red GCs. This is in stark contrast with the $<3\%$ contributed to the stellar halo by the same satellites (75% quantile).

It is interesting to note that, in MW mass galaxies, the median distribution of VMRs of satellites contributing to the stellar halo, to the accreted population of red GCs and to the accreted population of blue GCs are all systematically different from each other: the accreted GC population does

not really trace the assembly of the stellar halo. As already mentioned, the stellar halo is dominated by high VMR accretion events. Minor mergers become increasingly important for red and blue GCs. As we will show in the following, this implies that the spatial distribution and kinematic properties of these three halo populations should be expected to be different.

In this simple model, haloes with $\log M_{\text{host}}(z=0)/M_{\odot} = 12.3$ accrete a total of between 149 and 196 blue GCs, and 31 to 49 red GCs (25 and 75% quantiles for both populations). Given the simplistic hypotheses on which they are based, these figures should be taken as qualitative estimates. However, it is interesting to notice that the simplest possible combination of physical ingredients, i.e. Λ CDM assembly histories and the measured GC abundances (3) appear to produce $z=0$ GC populations that compare favorably with expectations. According to equations (3), a virial mass of $\log M_{\text{host}}(z=0)/M_{\odot} = 12.3$ corresponds to 83 red and 125 blue GCs (a scatter of 0.3 dex corresponds to approximately a factor of 2). Both total GC abundance (see e.g., Harris et al. 2017) and ratio between red and blue GC populations (Harris et al. 2015) are roughly reproduced.

2.2 Massive haloes

The case of haloes with virial mass $\log M_{\text{host}}(z=0)/M_{\odot} = 13.5$ is illustrated in the rightmost panel of Fig. 1. The relation between the abundance of blue GCs and halo mass is the least steep, so the fractional contribution of minor mergers is highest for blue GCs, as for the case of MW mass haloes. Between 39 and 55% of blue GCs (25 and 75% quantiles) are contributed by satellites with $\log M_{\text{sat}}/M_{\text{host}} < 1/50$.

Fig. 1 shows that the contribution of low-mass satellites to the accreted stellar halo of high-mass galaxies is also higher than in the case of MW-like haloes. This is a consequence of the break in the SHMR at $\log M_{\text{host}}(z=0)/M_{\odot} \sim 12$, and a well known result (e.g., Purcell et al. 2007; Naab et al. 2007; Cooper et al. 2013; Pillepich et al. 2014). Differently from the case of MW-mass galaxies, in which all populations have different median trends, here the median cumulative fraction of accreted material in stars and red GCs are very similar to each other for mass ratios $\log M_{\text{sat}}/M_{\text{host}} \gtrsim -1.2$. This corresponds to 65% of the contributions to these populations. In other words, in massive galaxies, a majority of the material in the accreted stellar halo and in the accreted population of red GCs often have similar progenitors. This provides a qualitative justification to the finding that red GCs often trace the distribution of stars not just in the center, but also out to large galactocentric distances in massive galaxies (e.g., Strader et al. 2011; Pota et al. 2013; Agnello et al. 2014). At these radii this behaviour can not be simply due to material formed *in situ*, and has to be related to the similar kinematical properties of accreted stars and red GCs. Note however, that the scatter in the distributions of VMRs is significant for both these populations, suggesting that this similarity may be loose in some systems. For completeness, the total number of accreted blue GCs estimated by this simple model is of between 2350 and 2950, and of between 850 and 1250 for red GCs (25 and 75% for both populations), again in rough agreement with the expectation for this halo mass (respectively 1770 blue GCs and 2360 red GCs).

Figure 2 concentrates on the size of the different con-

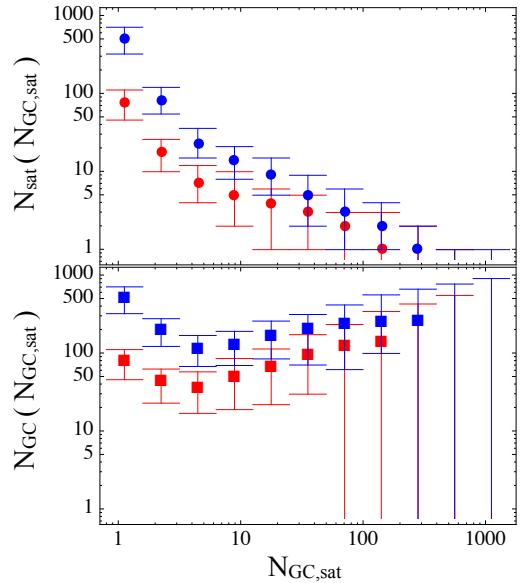


Figure 2. Upper panel: the total number of accreted satellites (N_{sat} , on the y axis) as a function of the number of GCs they contribute to the accreted population ($N_{GC,\text{sat}}$, on the x axis). Lower panel: the total number of accreted GCs (N_{GC} on the y axis) with progenitor satellites contributing $N_{GC,\text{sat}}$ GCs (on the x axis) to the accreted population. Red and blue points refer to the populations of red and blue GCs. Points indicate median values over a sample of 10^3 halo assembly histories, error bars extend between the 10 and 90% quantiles.

tributions to the accreted GC populations: $N_{GC,\text{sat}}$ on the x axis is the number of GCs contributed by an individual satellite. The top panel shows a demography of all contributions in terms of the number of accreted satellites that contribute $N_{GC,\text{sat}}$ GCs, since $z=6$. Points indicate medians, while the error bars extend between 10 and 90% quantiles of the distribution. Satellites that contribute >100 GCs are rare, for both blue and red GCs. Due to preponderance of low mass accretion events, in these simple models, there are on average more satellites contributing a single GC than satellites contributing $N_{GC,\text{sat}} > 1$. This is mirrored in the lower panel, which shows the total number of GCs accreted in a contribution of size $N_{GC,\text{sat}}$. Note that, if the upper panel plots the function $N_{\text{sat}}(N_{GC,\text{sat}})$, the lower panel is plotting $N_{GC} = N_{GC,\text{sat}} \times N_{\text{sat}}(N_{GC,\text{sat}})$. Poisson noise in the assembly histories is especially evident: high VMR mergers (e.g., $M_{\text{sat}}/M_{\text{host}} > 0.5$) are rare, but may contribute a large fraction of all GCs, introducing significant stochasticity. The number of GCs contributed individually or as part of small groups shows less scatter, and is consistently high in all assembly histories.

3 VIRIAL MASS RATIOS AND KINEMATICS

Amorisco (2017b) (hereafter NA17) has shown that, for Λ CDM accretion events, the satellite-to-host VMR is the most important single parameter to drive the kinematical properties of the material accreted in minor mergers. The efficiency of dynamical friction increases with VMR, so that massive satellites manage to sink deeper in the central regions of the host, and deposit their contributions closer

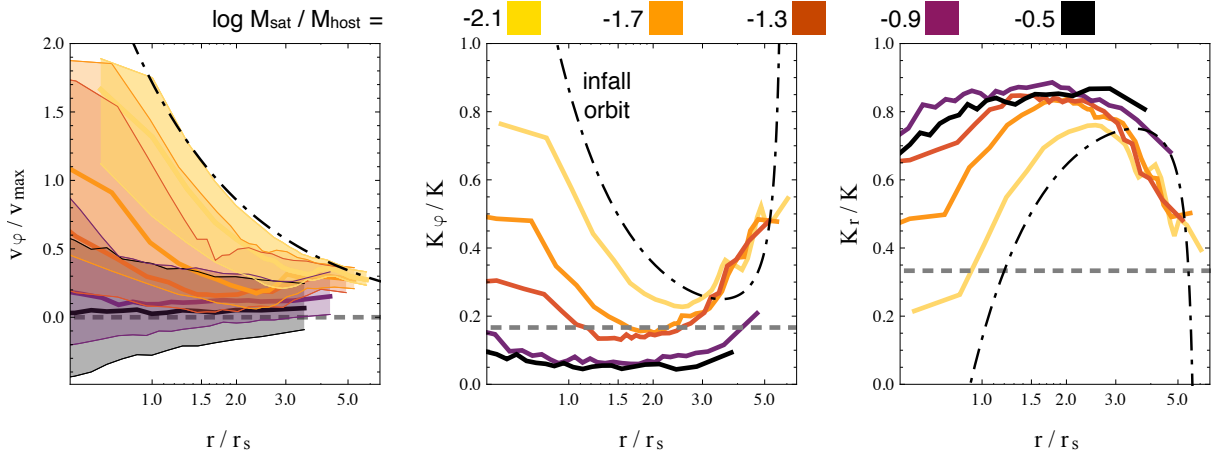


Figure 3. Kinematical properties of individual contributions from satellites with different virial mass ratio at accretion, color-coded as in the legend at the top. The shaded regions in the left panel extend between the 10 and 90% quantiles of the distribution of rotational velocities of particles contributed by individual satellites. The middle panel shows the fraction of the total kinetic energy in ordered rotation K_φ/K , the right panel the fraction in radial motion K_r/K . In all panels the dot-dashed black line describes the common infall orbit of all satellites, while the grey dashed line displays the expectation for a non rotating, isotropic population (after averaging over radius).

to the center. Instead, dynamical friction has little effect on the orbits of low-mass satellites, especially for VMRs $M_{\text{sat}}/M_{\text{host}} \lesssim 1/50$. As a result, a clear radial gradient emerges such that the VMR of the mean progenitor decreases with radius: i.e. minor mergers contribute preferentially at large galactocentric distances (see also [Rodríguez-Gomez et al. 2016](#)).

NA17 also shows that massive satellites have their orbits radialised by dynamical friction, to the point that almost all memory of the orbital properties at infall is lost for VMRs $M_{\text{sat}}/M_{\text{host}} \gtrsim 1/20$. Consequently, the material deposited by massive satellites has a strong radial bias. On the other hand, minor mergers are substantially less affected by radialization, and preserve a larger fraction of their orbital angular momentum. The mean orbital circularity of cosmological accretions is $j \sim 0.5$ (e.g., [Benson 2005](#); [Wetzel 2011](#); [Jiang et al. 2015](#), here j is the ratio of the orbital angular momentum J to the maximum angular momentum for the same orbital energy, $J_{\text{circ}}(E)$). Therefore, on average, the material contributed by low mass satellites has a considerable angular velocity (see e.g. Fig. 10 in NA17).

We take the isolated minor merger N-body simulations presented in NA17. These consider the mergers of two idealised spherical, non-rotating dark matter haloes with Navarro-Frenk-White density profiles (NFW, [Navarro et al. 1997](#)). The suite presented in NA17 considers a range of different structural and orbital parameters, and we refer the reader to that work for more details. For this paper, we use the runs corresponding to mean values for the satellite-to-host density contrast (i.e. mean dark halo concentration parameters for both host and satellite haloes), a fixed median circularity at infall of $j = 0.5$ and a fixed orbital energy at infall. We consider a range of values for the satellite-to-host VMR: $M_{\text{sat}}/M_{\text{host}} \in \{-2.1, -1.7, -1.3, -0.9, -0.5\}$. As discussed in NA17, the limits of this approach are analogous to those of the so called ‘particle-tagging’ technique (e.g., [Bullock et al. 2001](#); [Napolitano et al. 2003](#); [Bullock & Johnston 2005](#); [Cooper et al. 2010, 2013](#); [Ramos-Almendares et](#)

[al. 2017](#)), which are extensively discussed in the literature (see e.g., [Cooper et al. 2010](#); [Bailin et al. 2014](#); [Cooper et al. 2017](#), NA17). Here we use a tagging fraction of $f_{\text{tag}} = 8\%$.

The left panel of Fig. 3 shows the distribution of orbital velocities v_φ of material contributed by satellites with different VMR. The angle φ is the angle in the satellite’s orbital plane, r_s is the scale radius of the host NFW halo and v_{max} is its maximum circular velocity. The shaded regions extend between the 10 and 90% quantiles of the distribution and the colour-coding is as in the legend at the top. The kinematical properties of the accreted material display a clear gradient with VMR. Material contributed by massive satellites does not preserve coherent rotation, and is scattered in an approximately symmetric way with respect to the direction of the satellite’s orbital motion at infall, i.e. with respect to $v_\varphi = 0$. With decreasing VMR, more and more angular momentum is retained and the contributed material traces more closely the infall orbit itself, which is shown as a dash-dotted line.

The middle and right panels in the same Figure show the fraction of the total kinetic energy K associated with rotating motion in the φ direction, K_φ/K , together with the fraction in radial motion K_r/K . Lines display medians over the contributed material. Horizontal dashed lines show the expectation for the mean fraction of kinetic energy of a non rotating population with isotropic orbital distribution. The dash-dotted lines indicate the infall orbit. As in the case of the distribution in rotational velocity v_φ , the kinematical properties of material contributed by lower and lower VMR becomes more similar to the orbit of the progenitor satellite. With increasing VMR tangential motion decreases systematically due to dynamical friction, with a corresponding increase in radial bias.

3.1 LOSVDs and kurtosis

The kinematic properties illustrated in the previous Section characterize the material deposited by individual satellites.

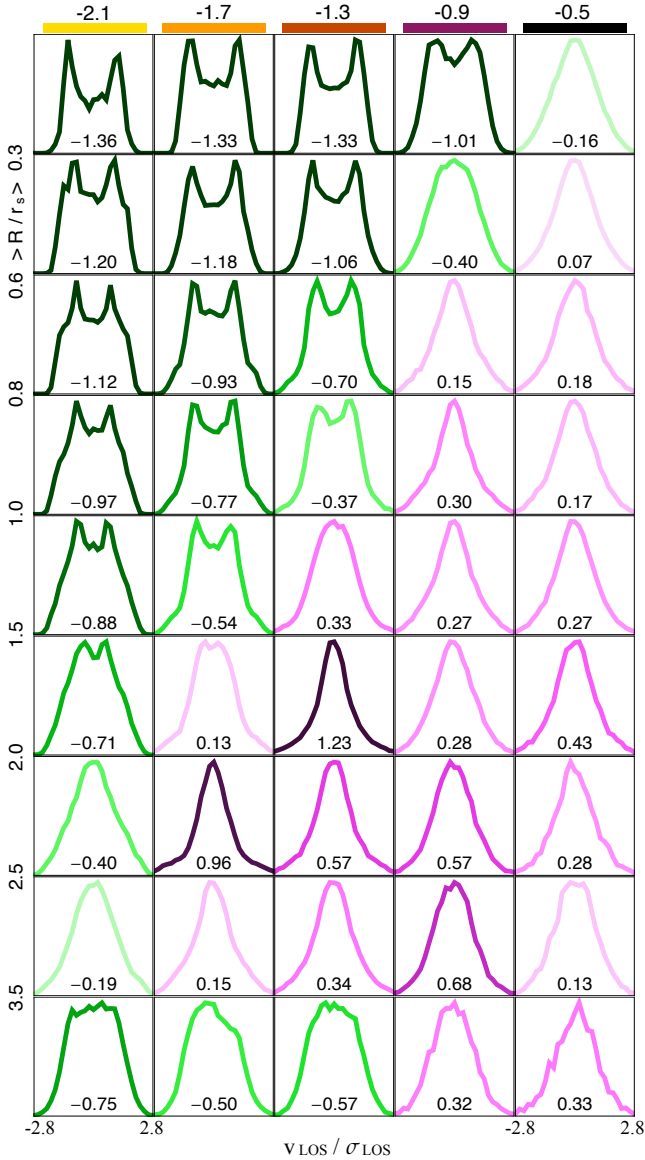


Figure 4. Line-of-sight velocity distributions for accreted populations contributed by satellites with identical satellite-to-host virial mass ratio. Each column refers to the virial mass ratio shown at the top. Different rows refer to different projected radial intervals. Individual line profiles are color-coded by the value of the kurtosis κ , which is indicated at the bottom of each panel.

Here we wish to focus on the LOSVDs obtained by superposing the contributions of multiple satellites. For the moment we ignore the cosmological setting (which will be introduced in Section 4) and for each VMR we superpose a large number of identical contributions, from identical satellites infalling on identical orbits with random directions. Figure 4 shows the resulting LOSVDs: different columns identify different mass ratios as indicated at the top, while different rows are for different projected circular annuli, in units of the characteristic radius of the host NFW profile, r_s . All LOSVDs are displayed in terms of the normalised LOS velocity $v_{\text{LOS}}/\sigma_{\text{LOS}}$, where σ_{LOS} is calculated in the same radial interval. Profiles are colour-coded according to the value of their kurtosis κ , which is also displayed at the

bottom of each panel. Green colours identify negative values of κ , while LOSVDs coloured in shades of pink have $\kappa > 0$. A diagonal colour divide is evident: negative values of the kurtosis are common for low VMRs and closer to the centre of the host. Positive values of the kurtosis become prevalent for increasing VMRs and at larger radii. For context, assuming mean concentration parameters (e.g., Ludlow et al. 2014), an NFW halo with $\log M_{\text{host}}(z=0)/M_{\odot} = 13.5$ has a scale radius r_s of $r_s \sim 70$ kpc ($r_s \sim 100$ kpc) at $z=1$ ($z=0$). Note that the radial range covered here is substantially larger than in typical observations.

This qualitatively shows that negative values of κ have their origin in the contribution of minor mergers. In particular, markedly double peaked LOSVDs are common in the upper-left corner. As showed in the previous Section, material contributed by minor mergers follows quite closely the progenitor’s orbit, with high angular velocity. Double peaks are then caused by the superposition of individual sub-populations rotating with random orientations. With increasing VMR, the degree of tangential motion in the contribution of each single satellites decreases, causing the double peaks to disappear. Higher virial mass ratios result in LOSVDs with heavy tails and sharper central peaks, as expected for material moving on radially biased orbits.

Across different VMRs, the kurtosis κ have a similar trend with radius. i) $\kappa(R)$ is increasing at small radii; ii) reaches a maximum that depends on VMR at a radius that decreases with VMR; iii) $\kappa(R)$ appears to decrease at large radii. This behaviour tracks orbital structure. At small (large) radii most contributed particles approach pericenter (apocenter), making double peaks more pronounced and lowering the value of the kurtosis. Due to dynamical friction, the radius of these turnaround points increases with decreasing VMR. Finally, as massive satellites shed material that fills much larger phase space volumes, radial gradients in $\kappa(R)$ are less pronounced for high the highest VMRs.

In Fig. 4 we have superposed the contributions of a large number of identical satellites. While illustrative, this choice makes the resulting LOSVDs unrealistic. The associated values of κ are somewhat extreme when compared to values usually achieved in the context of distribution function based dynamical modelling (e.g., Gerhard 1991, 1993; van der Marel & Franx 1993; Carollo et al. 1995; Bertin et al. 1997). For example, very sharp double peaks are apparent, due to artificially identical distributions of pericenters and apocenters. This effect is diluted in a cosmological context, where satellites accreted at different redshift deposit material with different orbital energies and at different radii around the host (e.g., Bullock & Johnston 2005; Cooper et al. 2010, NA17).

There is however a second genuine difference between the phase space distribution of halo populations contributed by minor mergers and the phase space distributions generally used for modelling the main stellar body of galaxies. The latter are usually required to generate density distributions that are monotonic with galactocentric distance, corresponding to monotonic distributions in energy. When seen in projection, these are characterized by a superior abundance of material moving with low LOS-velocity, and therefore more clearly bell-shaped LOSVDs. In turn, each minor merger contribution represents a coherent phase space pocket, with a tight and non-monotonic distribution in en-

ergy. Depending on the value of the VMR, this corresponds to a dearth of material with low energies and LOS-velocity, as well as to central density hole (see NA17).

4 THE KINEMATICS OF COSMOLOGICALLY ACCRETED GC POPULATIONS

We now combine the Λ CDM assembly histories presented in Section 2 (a subset of 200) to the minor merger simulations introduced in Section 3, to construct toy models of the GC populations cosmologically accreted by galaxies hosted by a halo with $\log M_{\text{host}}(z=0)/M_{\odot} = 13.5$. As done in Section 2, we track blue and red GCs accreted since $z=6$ separately, and assume that accreted satellites have deposited all of their GCs in the accreted halo of the host. We use N-body simulations with different VMRs to assign phase space coordinates to each GC at $z=0$, sampling randomly among the most bound satellite’s particles, up to a tagging fraction of 8%. We assume accretion events are uncorrelated, and that satellites infall from random directions. To account for redshift evolution, we scale r_s and v_{max} to the values of the host NFW halo at the accretion redshift, using our assembly histories and a mean mass-concentration-redshift relation (e.g., Gao et al. 2008; Ludlow et al. 2014). We do not expect such a simplified model to provide a realistic description of the accreted GC populations. Rather, this investigation is aimed to explore to what degree the combination of the fundamental ingredients of the process of cosmological assembly (i.e. Λ CDM assembly histories, gravitational dynamics and observed GC abundances) can reproduce the observed kinematic properties and trends of GC halo populations.

4.1 Edge-on kinematic maps by virial mass ratio

Figure 5 shows maps of the LOS kinematics of cosmologically accreted blue GCs. Different columns refer to sub-populations of GCs contributed since $z=6$ by satellites with different VMRs, with values as in the legend at the top. The corresponding maps for the red GCs would be essentially indistinguishable due to the small size of the adopted VMR bins². The maps show median values across a set of 200 individual assembly histories. The top row shows values of the LOS velocity v_{LOS} , the middle row shows velocity dispersion σ_{LOS} , the bottom row displays values of the kurtosis κ . Note that the radial scale is logarithmic, extending between 3 and 350 kpc as illustrated in the right-most panels. To preserve any rotation pattern, the displayed maps are edge-on projections. For each individual assembly history and bin in VMR, an edge-on projection is obtained by aligning with respect to the corresponding total angular momentum. In addition, symmetry with respect to the axis of rotation is assumed.

First, we notice that the kurtosis κ displays very similar patterns as those identified in Section 3.1. i) Negative values of κ are dominant for material contributed by minor mergers. ii) κ increases with VMR and is higher at larger

² Note that the full populations of blue and red GCs will still be different from each other due to the different relative contributions of the considered bins.

galactocentric radii. Both of these trends survive the ‘mixing’ process that accompany the cosmological setting, which causes material accreted at higher redshift to be deposited closer to the centre of the host halo.

Interestingly, the superposition of the contributions of multiple satellites may still result in coherent rotation, despite the assumption of uncorrelated infall directions. Negligible residual rotation is seen in the GC sub-population contributed by the satellites with the lowest or highest VMRs. In the former, the numerous individual contributions result in close to complete averaging. In the latter, each satellite deposits a non-rotating contribution, as shown in Fig. 3. At intermediate VMRs, however, material deposited by each individual satellite retains substantial rotation and the number of uncorrelated contributions is low enough that coherent rotation may survive. The mean rotation patterns seen in the averages of Fig. 5 are therefore dominated by the driving signal associated with the contribution of one single satellite, or to the fortuitous constructive superposition of a very small number of them. The significant scatter in the relations (3) may also help individual contributions to dominate within their VMR bin. Note however, that any residual rotation in the two bins $-1.9 < \log M_{\text{sat}}/M_{\text{host}} \leq -1.5$ and $-1.5 < \log M_{\text{sat}}/M_{\text{host}} \leq -1.1$ will likely not add up in a constructive way, as the chance of aligning angular momentum vectors is low.

Values of the LOS velocity dispersions are clearly decreasing with VMR, a consequence of the increasing efficiency of dynamical friction. Material sinking to the center loses energy and has therefore lower velocities (see also NA17). This results in radial segregation, as shown in Figure 6, displaying the cumulative distribution functions (cdfs) of the projected number counts of the different GC sub-populations. Thick lines are medians over the considered 200 assembly histories and the shaded regions extend between the 10 and 90% quantiles. The different sub-populations are radially ordered by VMR. Scatter around the median profiles increases with VMR, due to the increasing Poisson noise resulting from a smaller number of contributions for higher VMRs. Blue GCs accreted by satellites with $\log M_{\text{sat}}/M_{\text{host}} > -0.7$ have a half-number radius R_h between 13 and 43 kpc (10 and 90% quantiles); between 135 and 185 kpc for $\log M_{\text{sat}}/M_{\text{host}} < -1.9$. The corresponding values for red GCs are very similar: the sub-populations of red and blue GCs defined by VMR of the contributing satellites are essentially indistinguishable. It is their different fractional contribution that causes any differences in the global kinematic properties of blue and red GCs, which we analyze in the following.

4.2 Mean projected kinematics

Figure 7 shows the LOS kinematic profiles of the full blue and red populations of accreted GCs. The sets of lines show the 25, 50 and 75% quantiles over our set of 200 assembly histories. Full lines include an averaging over inclinations (with respect to the angular momentum of the full blue GC accreted population), which we perform by using 20 random viewing angles for each individual halo. From left to right, columns display respectively: maximum rotational velocity $v_{\text{LOS,max}}$, velocity dispersion σ_{LOS} , kurtosis κ and cdf of the number counts.

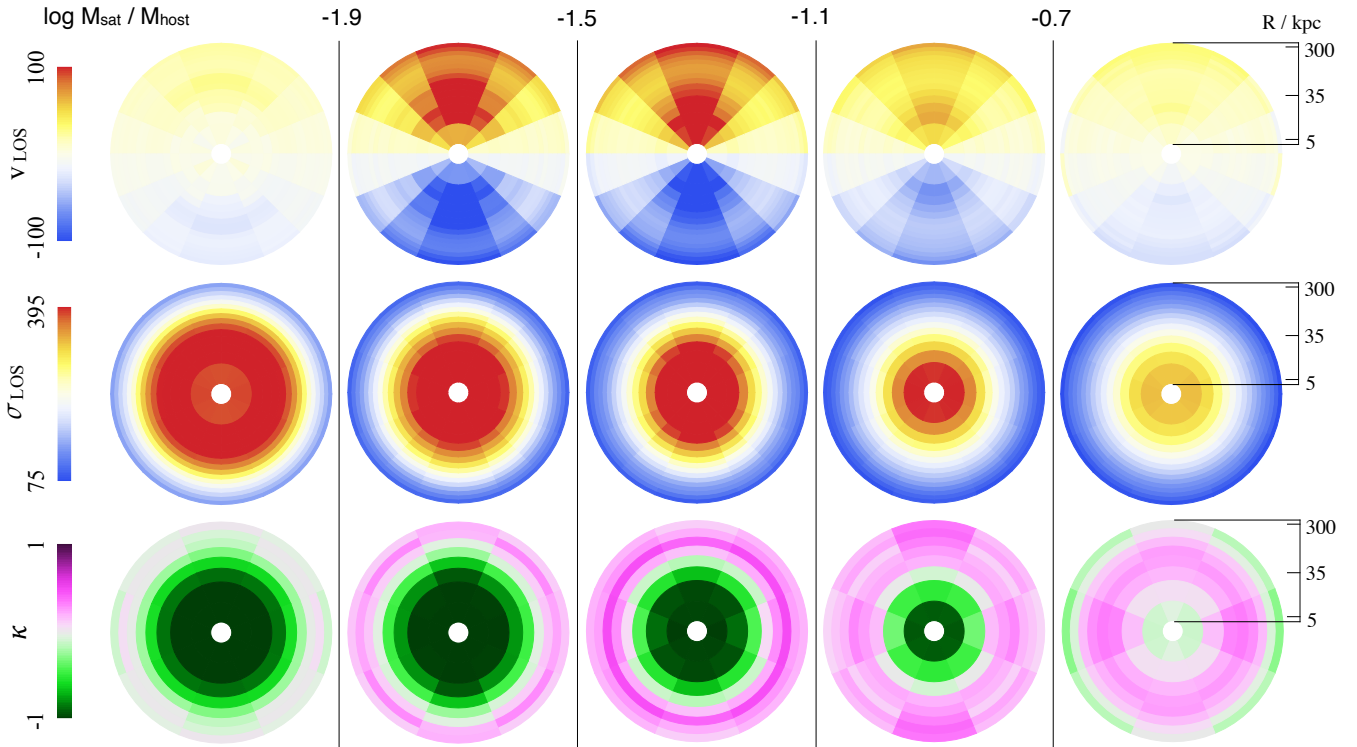


Figure 5. Edge-on projected kinematic maps for the accreted blue GC population (medians over 200 accretion histories), for a massive galaxy with $\log M_{\text{host}}(z=0)/M_{\odot} = 13.5$. Contributions of different satellites are grouped according to the value of the virial mass ratio at accretion. The legend at the top of the figure indicates the limiting values that define the considered bins in virial mass ratio.

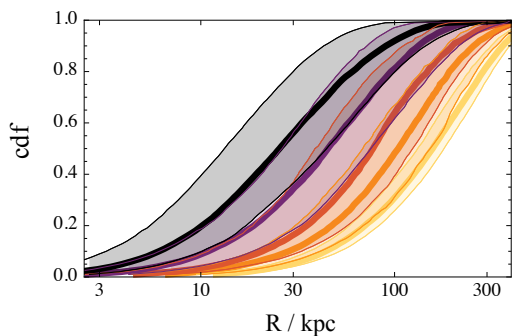


Figure 6. The cumulative distribution for the projected number counts of the sub-populations of cosmologically accreted GCs contributed by satellites with different mass ratios. Color-coding as in Fig. 4. The shading extends between the 10 and 90% quantiles over the studied set of 200 assembly histories.

We mimic the measurement procedures used with real data (e.g., Pota et al. 2013): values of $v_{\text{LOS,max}}$ are obtained by performing azimuthal fits in different radial bins, assuming a simple sinusoidal dependence,

$$v_{\text{LOS}}(R, \theta) = v_{\text{LOS,max}}(R) \cos(\theta - \theta_0). \quad (4)$$

To simulate the effects of differing LOS orientations, this procedure is repeated for 20 random viewing angles. Full lines display quantiles over the full set of angles, dashed lines simulate a close to edge-on projection, by showing quantiles over the subset of those 10 angles that result in the highest values of $v_{\text{LOS,max}}$.

The two rows in Fig. 7 focus on a total of 100 differ-

ent assembly histories each, dividing the full set according to the fraction of GCs contributed by satellites with $\log M_{\text{sat}}/M_{\text{host}} > -0.7$. As seen in Fig. 2, despite the importance of minor mergers, accretion events with high VMR are highly stochastic, and may contribute a substantial fraction of the accreted GC population. In 50% of our assembly histories, the fraction of blue GCs contributed by satellites with $\log M_{\text{sat}}/M_{\text{host}} > -0.7$ is < 0.21 : $f_{50}(\log M_{\text{sat}}/M_{\text{host}} > -0.7) = 21\%$. This threshold separates the assembly histories contributing to the top/bottom panels of Fig. 7. Stochasticity, however, is such that, in a 5% of all assembly histories, satellites with $\log M_{\text{sat}}/M_{\text{host}} > -0.7$ contribute as much as 57% of all blue GCs: $f_{95}(\log M_{\text{sat}}/M_{\text{host}} > -0.7) = 57\%$.

There are few aspects worthy of notice.

- First of all, the accreted blue GCs are systematically more spatially extended than the red GCs, in both families of assembly histories. At the same time, the velocity dispersion of blue GCs stays consistently higher than that of red GCs. Both of these aspects are in agreement with observations and, in these models, are a natural consequence of the slightly different abundances prescribed by eqns (3). Blue GCs have a higher fractional contribution from minor mergers, and therefore more extended density distributions and higher velocity dispersions.

- Slightly more in detail, over the 200 explored assembly histories, we find that the 10-to-90% quantile range for the projected half-number radius of the blue GC population is 60 – 111 kpc, while the red GCs have 45-94 kpc. These correspond respectively to intervals of $\approx 9 - 17\%R_{\text{vir}}$ and

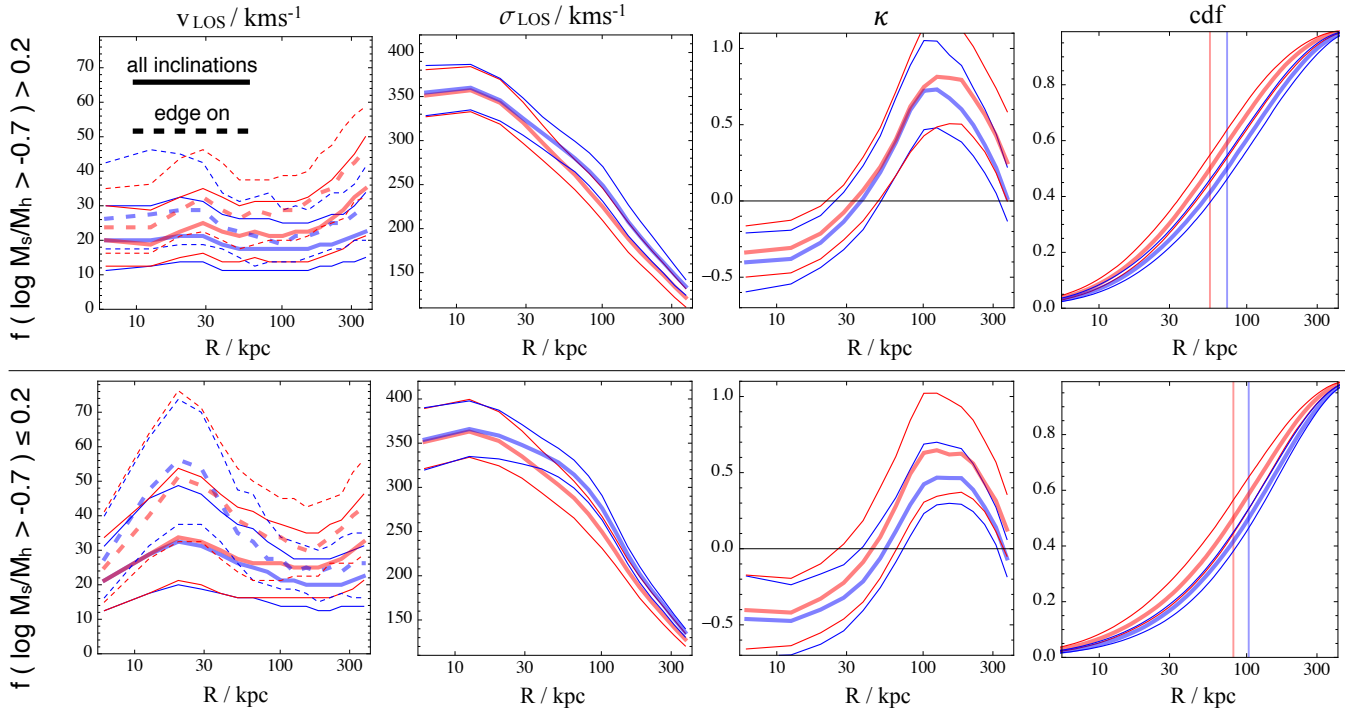


Figure 7. Mean projected kinematics for the cosmologically accreted blue and red GC populations, as a sum over all contributing satellites. The two rows of panels display the effect of different accretion histories: upper (lower) panels refer to assembly histories in which accretion events with $\log M_{\text{sat}}/M_{\text{host}} > -0.7$ contribute $> 20\%$ ($\leq 20\%$) of all blue GCs, corresponding to a 50% of all studied assembly histories. In each panel, full lines average over viewing angles. Dashed lines in the left panel refer to viewing angles close to edge-on with respect to the total angular momentum of the accreted blue GCs (see text for details). In each row, the first panel shows the maximum line-of-sight rotational velocity, the second panel displays line-of-sight velocity dispersion, the third panel shows kurtosis, the fourth panel displays the cumulative distribution function for the projected number counts. In all cases, the sets of lines display the 25, 50 and 75% quantiles of the distribution, over different accretion histories and inclinations. The vertical lines in the right-most panel identify the half-count radius.

$\approx 7 - 14\%R_{\text{vir}}$, in good quantitative agreement with recent compilations by [Hudson & Robison \(2017\)](#) and [Forbes \(2017\)](#).

- The median radial profile of the kurtosis κ has a well defined shape, with preferentially negative values for both blue and red GCs within ~ 40 kpc (~ 50 kpc in the bottom row, when minor mergers are dominant). Then, κ quickly increases towards positive values at larger radii. If the contribution of high VMR accretion events is substantial, higher values of κ are achieved (top row).

- Differences in the kinematical properties between the bottom and top row are systematic, but limited with respect to the scatters introduced by the details of the assembly histories. Residual rotation is stronger when minor mergers are dominant, and the velocity dispersion of both populations is consistently higher.

- The most noticeable difference between the bottom and top rows is in the spatial distributions. Vertical lines in the rightmost panels indicate half-count radii, which are significantly larger when the contribution of minor mergers is higher. We can not make a direct comparison between these predicted sizes and observations, as these models do not account for the contribution of the *in situ* GC population. We notice however that the half-count radii displayed in Fig. 7 compare well with observations of galaxies with similar halo mass (e.g., [Forbes 2017](#); [Hudson & Robison 2017](#)). The cor-

relation between size and assembly history is also especially promising.

Finally, we note that rotation patterns in the GC populations of individual haloes are often twisted, i.e. the position angle $\theta_0(R)$ as defined in eqn. (4) varies significantly with radius. This is the case for both blue and red GC populations. At the same time, red and blue GCs often have different kinematic position angles. This is a consequence of the stochastic nature of residual rotation in these simple models (see also e.g., [Moody et al. 2014](#)). As mentioned in Section 4.1, coherent rotation is driven by the contributions of satellites with intermediate VMR and survives only in the absence of efficient averaging. Due to both intrinsic and Poisson noise on the relations (3), it is not unlikely that the rotation signal of blue and red GC populations is dominated by the contribution of different satellites, with likely misaligned angular momentum vectors.

4.3 Orbital anisotropy

We have shown that negative values of the kurtosis are a natural product of the residual tangential motion of the contributions of minor mergers and that they are ubiquitous in the central regions for the accreted population of GCs. Here, we address orbital structure. Figure 8 shows the anisotropy profile $\beta(r)$ of the sub-populations of the accreted blue GCs

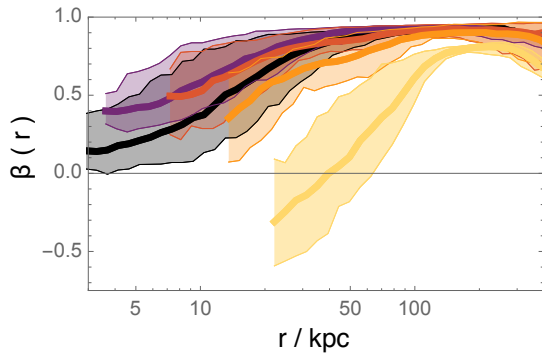


Figure 8. Profiles of the anisotropy parameter $\beta(r)$ for the GC sub-populations as in Fig. 5 and 6. Lines indicate median values and the shading extends between the 10 and 90% quantiles over the studied set of 200 assembly histories. Colour-coding as in Fig. 4 and 6.

defined by VMR of the parent satellite, as in Figs. 5 and 6, with the same colour-coding. Thick lines show medians over our 200 assembly histories, shaded regions extend between the 5 and 95% quantiles of the distribution.

For all VMRs, anisotropy profiles increase towards large radii, with very high values of β reached at $r \gtrsim 100$ kpc. Due to the segregation induced by dynamical friction, the profiles relevant to low VMRs do not extend to the very central regions of the host, where not enough GCs are contributed. Except for the contribution of satellites with $\log M_{\text{sat}}/M_{\text{host}} < -1.9$, the other subpopulations display a positive β over the entire radial range. In the very central regions, the anisotropy of the sub-population contributed by the highest VMR satellites is mildly radial, $\beta(< 20 \text{ kpc}) \sim 0.3$. This value increases for intermediate VMRs, but quickly decreases to negative values of β for the subpopulation with the lowest VMR. Although the scatter is considerable, we find that the superposition of GCs cosmologically accreted from satellites with $\log M_{\text{sat}}/M_{\text{host}} < -1.9$ is approximately isotropic at $r \sim 40$ kpc and *tangentially biased* at smaller radii. Values of the anisotropy that are as low as $\beta \sim -0.5$ are within the 5% quantile. This tangential bias, however, is shared by only a very small fraction of the GCs in this sub-population: as mentioned in Sect. 4.1, the half-count radius of the GCs accreted from satellites with $\log M_{\text{sat}}/M_{\text{host}} < -1.9$ is $R_{\text{h}} > 135$ kpc in 90% of cases. Only a fraction of 8% is at $R < 40$ kpc. While tangential anisotropies are not uncommon in the very central regions for the sub-population contributed by minor mergers, this is not predicted to be a dominant behaviour.

Figure 9 shows the anisotropy profiles of the full populations of red (left panels) and blue GCs (right panels). Full lines show medians, the shading extends between the 5 and 95% quantiles of the distribution. As in Fig. 7, the top row collects the 100 assembly histories in which the fractional contribution to the blue GC population of satellites with $\log M_{\text{sat}}/M_{\text{host}} > -0.7$ is < 0.21 . The bottom row has the complementary set with $f(\log M_{\text{sat}}/M_{\text{host}} > -0.7) \geq 0.21$. The median anisotropy of the GC sub-populations defined by VMR are also shown, for comparison, with the same colour-coding as in Fig. 8. We find that both red and blue GC populations have predominantly radial anisotropy, and that any dependence on the assembly history is minor. For

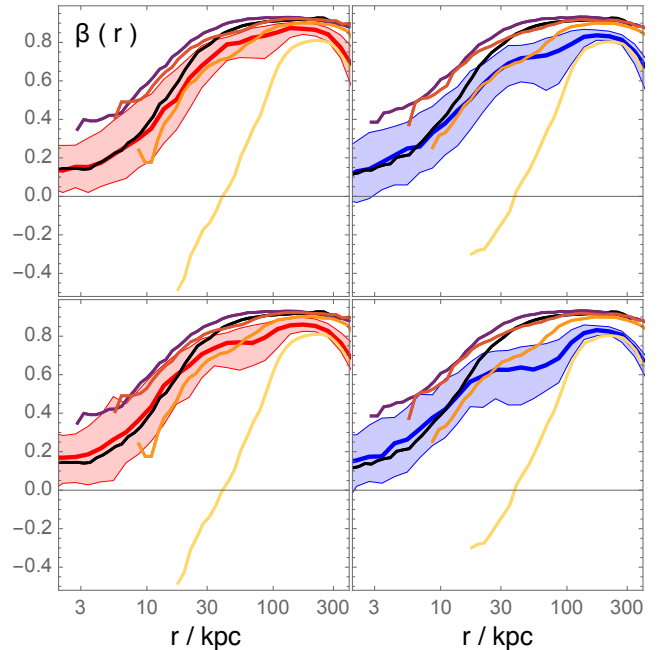


Figure 9. The anisotropy profiles of the cosmologically accreted red (left panels) and blue (right panels) GC populations. Full lines show medians, the shading extends between the 5 and 95% quantiles of the distribution. Top and bottom row are for different assembly histories, as in Fig. 7. For comparison, panels also display the anisotropy profiles of the sub-populations defined by virial mass ratio, as in Fig. 8.

all practical purposes, accreted red and blue populations have very similar anisotropy profiles: β is very mildly positive in the central regions ($r \lesssim 10$ kpc), and then displays a sustained increase towards larger radii, with little scatter across different assembly histories. The anisotropy profiles of the full red and blue population can be seen to follow the profile of the subpopulation with the highest VMR in the centre, and of the population with the lowest VMR in the outermost regions, where they respectively dominate. Not enough GCs contributed by satellites with $\log M_{\text{sat}}/M_{\text{host}} < -1.9$ appear to be present in the very central regions to result in a tangentially biased orbital structure.

5 SUPERPOSING ACCRETED AND ‘IN-SITU’

So far, we have dealt with the population of accreted GCs. As we have seen, once a Λ CDM framework has been chosen, their spatial distribution and kinematic properties can be constructed quite easily. There is a very limited number of free parameters to fix: by concentrating on the accreted population alone, the current analysis remains a self-contained one. However, a direct comparison with observations would of course require a model for the population of ‘in-situ’ GCs. Unfortunately, it is not currently straightforward to derive the kinematic properties of the in-situ population in a constructive manner, as done for the accreted population, as a model for its formation mechanism(s) is not readily available, and in fact currently the subject of intense study (see e.g., [Forbes et al. 2018](#), and references therein). We can certainly assume that the in-situ population is negligible in

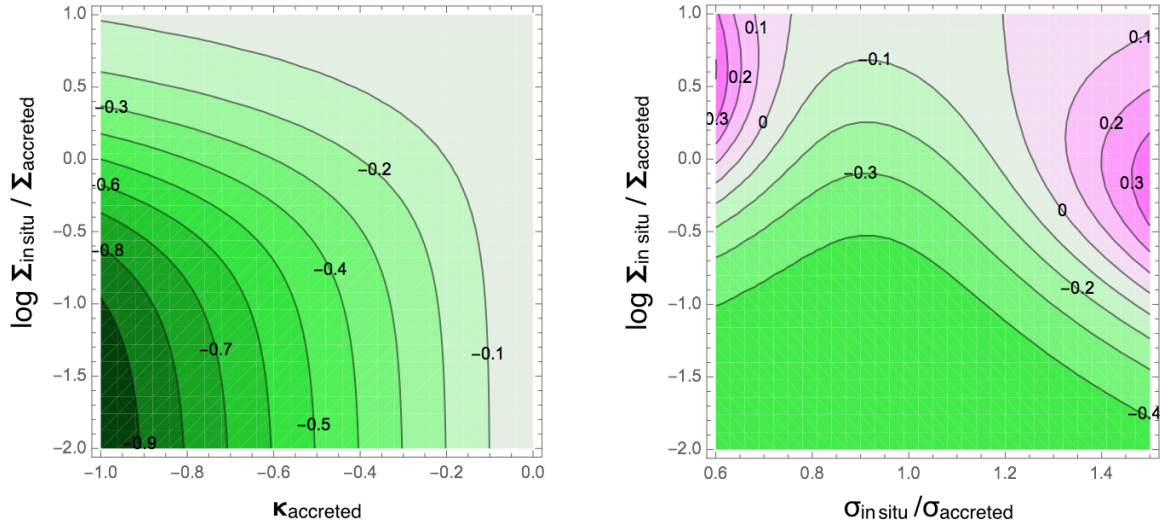


Figure 10. The kurtosis κ of a population including an in situ and an accreted component. (the LOSVD of the in situ component is assumed Gaussian). The left panel shows values of the kurtosis from the superposition of an accreted population with varying κ_{accreted} (on the x axis) and an in situ population with varying relative normalization (on the y axis). The LOS velocity distribution of the in situ component is kept fixed at $\sigma_{\text{in situ}} = \sigma_{\text{accreted}}$. The right panel shows values of the kurtosis from the superposition of an accreted population with $\kappa_{\text{accreted}} = -0.5$ and an in situ population with varying $\sigma_{\text{in situ}}$ and relative normalization (respectively, on the x and y axis).

the outer regions, but to explore how the two components combine in the total observed GC population requires a full characterisation of both.

In the absence of a constructive model for the in-situ component a number of arbitrary choices become necessary. Even under the most extreme simplification, we would need to explicitly fix: i) the total abundance of GCs formed in-situ (the fraction with respect to the abundances prescribed by eqns 3); ii) its half-number radius and detailed density profile; iii) its full orbital structure, which includes its anisotropy as well as whether it has any ordered rotation. A specific formation mechanism would provide a prediction for the quantities above, an alternative possibility is to explore a range of choices for these. Such a detailed exploration goes beyond the scope of the current study, but we can still gain substantial insight using a simplified framework. What we are most interested in here is in how the properties of the LOS velocity distribution of the accreted population get ‘diluted’ by those of the in-situ population. In particular, in whether the negative values of κ survive the superposition of an in-situ population.

We consider the observed LOSVD, $f_{\text{LOS},\text{tot}}(v, R)$, i.e. the superposition

$$\Sigma_{\text{tot}}(R)f_{\text{LOS},\text{tot}}(v, R) = \Sigma_{\text{ac}}(R)f_{\text{LOS},\text{ac}}(v, R) + \Sigma_{\text{in}}(R)f_{\text{LOS},\text{in}}(v, R). \quad (5)$$

Here we have taken that all LOSVDs $f_{\text{LOS},j}(v, R)$ (for all j) are normalised to unity, $\int f_{\text{LOS},j}(v, R)dv = 1$, and that $\Sigma_j(R)$ is the surface density of the different components. We have seen that negative values of κ_{ac} are the norm in the inner regions ($R \gtrsim 40$ kpc) for the accreted population. On the other hand it is plausible to assume that the LOSVD of the in situ population is close to normal, with $\kappa_{\text{in}} \approx 0$. As a simple representative case we take that $f_{\text{LOS},\text{in}}(v, R)$ is exactly Gaussian, with zero mean. With this hypothesis, Figure 10

explores the kurtosis κ_{tot} of the observed LOSVD $f_{\text{LOS},\text{tot}}$ obtained by superposing an accreted population and an in-situ population with different properties.

The left panel explores the case of different values of the kurtosis κ_{ac} of the accreted population (on the x axis) and of a varying relative contribution of the in-situ component, $\log \Sigma_{\text{in}}/\Sigma_{\text{ac}}$ (on the y axis). We have assumed that $\sigma_{\text{ac}} = \sigma_{\text{in}}$ and, for the LOSVD of the accreted population we have used the family of symmetric, positive definite, LOSVDs constructed in Amorisco & Evans (2012). Where the accreted component dominates, $\Sigma_{\text{in}} \ll \Sigma_{\text{ac}}$, $\kappa_{\text{tot}} \approx \kappa_{\text{ac}}$, as can be expected in the outer regions of the halo. The negative values of κ_{ac} get progressively diluted by an increasing in-situ component. However, the left panel of Fig. 10 shows that κ_{tot} remains negative even when the contribution of the in-situ component is comparable to the one of the accreted component, and in fact even when higher.

Finally, in the right panel we relax the hypothesis that $\sigma_{\text{ac}} = \sigma_{\text{in}}$: while it is likely that $\sigma_{\text{ac}} \approx \sigma_{\text{in}}$, the two values will in general be different, as the two components satisfy different equilibrium conditions. As a representative value, we fix $\kappa_{\text{ac}} = -0.5$, which we have found to be typical for the innermost regions of the accreted population (see Fig. 7). Once again, we see that the contribution of an in-situ population acts to dilute the negative kurtosis of the accreted population. However, in most of the parameter space $\kappa_{\text{tot}} \gtrsim 0$.

Instead of restricting ourselves to specific kinematical models, here we have explored the kurtosis resulting from the superposition of two different LOSVDs, covering a region of parameter space that plausibly encompasses a variety of useful cases. A more detailed analysis would be useful to better elucidate the interplay between the kinematic properties of in-situ and accreted population, in particular when these are required to both be in equilibrium. On the other hand, the exercise above already shows that, in the presence

of a significant fraction of accreted GC population, negative values of the kurtosis are especially resilient. Fig. 10 demonstrates that, where $\kappa_{ac} \lesssim 0$, it is highly likely that the observed kurtosis κ_{tot} is also negative if $\Sigma_{in} \lesssim \Sigma_{ac}$. The fact that negative values of the kurtosis are indeed observed for κ_{tot} , compatibly with our predictions for κ_{ac} , would appear to suggest that the accreted GC population represents a sizable fraction of the total also at intermediate radii, $10 \lesssim R/\text{kpc} \lesssim 40$. This is also compatible with the fact that our accreted-only GC abundances do not fall short of the observed values (Sect. 2), and that the predicted half-number radii compare well with observations (Sect. 4.2).

6 DISCUSSION AND CONCLUSIONS

In this paper we have investigated the kinematical properties of the GC populations assembled through hierarchical merging around massive galaxies. Our set up is purposely simplistic, and only accounts for the following fundamental ingredients: Λ CDM assembly histories, gravitational dynamics and measured relations between GC abundances and dark matter halo mass. This is instrumental to highlighting the possible need for any additional physical processes that are not accounted for in this work.

The ingredients above imply that the halo populations of accreted GCs have systematically different progenitors with respect to the stellar halo. This is due to the very different proportions with which accreted satellites contribute stars and GCs per unit of contributed dark matter. Because of the steepness of the SHMR, the stellar halo is dominated by the contributions of satellites with high VMR, which are strongly affected by dynamical friction. In contrast, if GC abundances are approximately proportional to halo mass, minor mergers are substantially more important in building up the GC halo populations. Since the material deposited by minor mergers has different kinematic properties from the one contributed by satellites with high VMR, the accreted GC populations do not in general trace the stellar halo. However, in hosts with $\log M_{\text{host}}(z=0)/M_{\odot} = 13.5$, approximately 65% of material in the stellar halo and in the accreted population of red GCs have been deposited by satellites with similar distributions of VMRs. This makes red GCs a better tracer of the stellar halo. In turn, the contributions to the accreted population of blue GCs are systematically biased towards satellites with lower VMRs. In 75% of Λ CDM assembly histories, the fraction of the accreted population of blue GCs contributed by satellites with $M_{\text{sat}}/M_{\text{host}} < 1/50$ at accretion is $> 39\%$ ($> 30\%$) for galaxies hosted by haloes with $\log M_{\text{host}}(z=0)/M_{\odot} = 13.5$ ($\log M_{\text{host}}(z=0)/M_{\odot} = 12.3$).

With respect to the accreted stellar halo, the fingerprints of the increased importance of minor mergers for the halo GC populations are: i) a more extended spatial distribution and ii) an increased degree of tangential motion. Even between red and blue GCs, differences in the relation between halo mass and GC abundance are sufficient to make the spatial distribution of blue GCs systematically more extended than the one of red GCs (half-number projected radius in the interval 9-17% R_{vir} for the blue GCs and 7-14% R_{vir} in 80% of cases), as well as to make the velocity dispersion of the former systematically higher. The increased

degree of tangential motion makes LOSVDs with negative kurtosis a distinctive trait of the increased contribution of satellites with low VMRs, in no contradiction with the accretion picture.

The kurtosis profiles of our toy-model accreted GC populations are negative in the central regions ($\kappa(R < 40 \text{ kpc}) \lesssim 0$), and turn to positive values at larger radii, for both blue and red GCs. The galaxy-to-galaxy scatter is significant and details of each system depend on the specific assembly history. In those regions where the accreted population has $\kappa \lesssim 0$ the observed kurtosis can be expected to preserve a negative sign as long as the in-situ contribution is not largely dominant. This justifies the fact that our predicted kurtosis profiles agree quite well with those observed (e.g., Pota et al. 2013).

These negative values of the kurtosis, however, do not correspond to tangentially biased orbital distributions. The cosmologically accreted populations of GCs constructed using our set of simplifying hypotheses have anisotropy profiles that increase from mildly radial in the central regions ($\beta(r < 10 \text{ kpc}) \sim 0.2$) to strongly radially anisotropic at large radii ($\beta(r > 30 \text{ kpc}) \gtrsim 0.6$). This confirms that the correspondence between kurtosis and anisotropy is only qualitative. A number of counterexamples to this correspondence are known in the literature (e.g., Gerhard 1993; van der Marel & Franx 1993; Napolitano et al. 2014), here we have provided an additional example of an equilibrium population with $\kappa < 0$, but $\beta \gtrsim 0$ at some radius. We attribute this to the phase space properties of the material accreted from minor mergers, which is highly clumpy in the space of the integrals of the motion (see also NA17). We find that the sub-population of cosmologically accreted GCs with $\text{VMR} \log M_{\text{sat}}/M_{\text{host}} < -1.9$ is tangentially biased at radii $r \lesssim 40 \text{ kpc}$, where GCs are mainly approaching the pericenter of the cosmological infall orbits of their progenitor satellites. Values of β can be as low as ~ -0.5 . However, at these radii, the contribution of satellites with higher virial mass ratios is dominant in our models, and in fact drives the anisotropy of the full GC population, which remains positive in more than 90% of cases.

6.1 Comparison with dynamical analyses

Measuring the orbital structure of pressure supported systems is a notoriously difficult task, due to strong model degeneracies. The infamous degeneracy between mass and anisotropy makes it difficult to disentangle the orbital structure of the tracer population from the profile of the embedding gravitational potential, as well as from the details of density profile of the tracers themselves (see e.g., Gerhard 1993; Binney & Tremaine 2008; Evans et al. 2009; Mamon et al. 2013, and references therein). Use of the higher moments of the LOSVD is helpful, though not always possible in dynamical analyses of GC populations, due to the limited number of available tracers (see e.g., Amorisco & Evans 2012). As a consequence, literature results on the orbital structure of GC populations are mixed (see e.g., Agnello et al. 2014; Napolitano et al. 2014; Zhu et al. 2014, 2016; Zhang et al. 2015; Pota et al. 2015; Oldham & Auger 2016; Wasserman et al. 2017). Additionally, a direct comparison with our results is not straightforward as many analyses have adopted models with radially constant orbital structure (see

however [Napolitano et al. \(2014\)](#) for an example of dynamical modelling with non-constant anisotropy). It is unclear whether a constant value of β may correctly describe our model populations, and what value of β would be inferred as a result. However, some studies have inferred a strong tangential orbital bias, which, despite these possible biases, appears difficult to reconcile with our simple models.

There is a number of mechanisms that may possibly be responsible for this discrepancy. For instance, the following two physical processes, which we have not accounted for, may alter the kinematics of the GC populations in the central regions of the host.

- First and foremost, we have neglected the contribution of GCs formed within the host halo itself, or formed during mergers (e.g., [Kruijssen et al. 2012](#)) rather than simply accreted. These may be dominant in the central regions and our model can not predict their kinematics. We have shown that an in-situ component is very unlikely to entirely erase the signal for a negative kurtosis, but we have not analysed how the in-situ component would affect the actual orbital structure and anisotropy of the full GC population. The orbital distribution of material formed *in situ* is usually less radially biased than the one of material that is cosmologically accreted (e.g., [Röttgers et al. 2014](#)). Additionally, these GCs may display disk kinematics, as seen in M31 (e.g., [Caldwell & Romanowsky 2016](#)), mimicking a tangentially biased orbital structure.

- Second, we have ignored the possibility that some GCs may have been shredded by the tides after they are accreted onto the host. GCs that reach closer to the centre are more easily disrupted, so that, as discussed in a number of works (e.g., [Bahcall & Wolf 1976](#); [Pota et al. 2013](#); [Agnello et al. 2014](#); [Wasserman et al. 2017](#)), GC disruption may cause a systematic depletion of GCs on radial orbits, possibly altering the orbital distribution.

It remains however unclear whether the latter effect may reconcile the present discrepancy. GC disruption is certainly a relevant process for low mass GCs (e.g., [Gnedin & Ostriker 1997](#); [Baumgardt 1998](#); [Vesperini & Heggie 1997](#); [Vesperini et al. 2003](#); [Peng et al. 2008](#); [Georgiev et al. 2010](#); [Kruijssen et al. 2012](#); [Gnedin et al. 2014](#); [Mieske et al. 2014](#)), but the accreted populations considered here only include those GCs that may survive in the contributing satellites. Observations in the MW suggest that some GCs that likely have an accretion origin may indeed experience tidal disruption (e.g., [Odenkirchen et al. 2003](#); [Grillmair & Dionatos 2006](#)). On the other hand, our model does not clearly overestimate GC abundances, which would suggest that the fraction of GCs destined to disruption *after accretion* is not substantial in our populations. This is supported by recent numerical simulations, which find that tides are in fact stronger in low mass hosts than are in massive galaxies ([Brockamp et al. 2014](#); [Zonoozi et al. 2016](#)).

In addition, both of the mechanisms above can only be effective in the central regions of the host: it appears difficult that they could significantly alter the strong radial bias displayed by our models at large radii. Therefore, observations of any signal for a tangential anisotropy at large galactocentric radii are especially interesting. Despite the significant halo-to-halo scatter, our models are uniformly strongly radial at large radii. These observations therefore raise the

question of whether a tangential anisotropy may be reproduced in a Λ CDM scenario by relaxing some of the hypotheses made here. For example, our models assume that most cosmological accretion events have intermediate circularity at infall ($j \sim 0.5$), and that this value is approximately independent of mass ratio (e.g. [Benson 2005](#); [Wetzel 2011](#); [Jiang et al. 2015](#)). As the material contributed by minor mergers best preserve memory of their infall orbit, the observed signal for tangential orbits may suggest differences in the orbital properties at infall. In future work, it would be interesting to explore whether a bias towards higher circularities for minor mergers may in fact produce accreted GC populations that are less radially biased, or even tangentially biased at large radii.

To conclude, many fundamental properties of the kinematics of GC populations around massive galaxies appear to be simply interpreted as a direct consequence of the important role of minor mergers. In particular, we have shown that there is no contradiction between the accretion scenario and the observed negative values of the kurtosis, which are instead ubiquitous when accretion events with low VMRs are important. It will be interesting to compare the results of this work with those of future kinematical analyses.

ACKNOWLEDGEMENTS

It is a pleasure to thank Jean Brodie, Duncan Forbes, Eric Peng and the Santa Cruz SAGES group for stimulating discussions.

REFERENCES

- Abadi, M. G., Navarro, J. F., & Steinmetz, M. 2006, *MNRAS*, 365, 747
- Agnello, A., Evans, N. W., Romanowsky, A. J., & Brodie, J. P. 2014, *MNRAS*, 442, 3299
- Amorisco, N. C., & Evans, N. W. 2012, *MNRAS*, 424, 1899
- Amorisco, N. C. 2017a, *MNRAS*, 469, L48
- Amorisco, N. C. 2017b, *MNRAS*, 464, 2882
- Bahcall, J. N., & Wolf, R. A. 1976, *ApJ*, 209, 214
- Bailin, J., Bell, E. F., Valluri, M., et al. 2014, *ApJ*, 783, 95
- Baumgardt, H. 1998, *AA*, 330, 480
- Benson, A. J. 2005, *MNRAS*, 358, 551
- Behroozi, P. S., Wechsler, R. H., & Conroy, C. 2013, *ApJ*, 770, 57
- Bertin, G., Leeuwijn, F., Pegoraro, F., & Rubini, F. 1997, *AA*, 321, 703
- Binney, J., & Tremaine, S. 2008, *Galactic Dynamics: Second Edition*, by James Binney and Scott Tremaine. ISBN 978-0-691-13026-2 (HB). Published by Princeton University Press, Princeton, NJ USA, 2008.,
- Blakeslee, J. P., Tonry, J. L., & Metzger, M. R. 1997, *AJ*, 114, 482
- Boylan-Kolchin, M. 2017, *MNRAS*, 472, 3120
- Brockamp, M., Küpper, A. H. W., Thies, I., Baumgardt, H., & Kroupa, P. 2014, *MNRAS*, 441, 150
- Brodie, J. P., & Strader, J. 2006, *ARAA*, 44, 193
- Brodie, J. P., Usher, C., Conroy, C., et al. 2012, *ApJL*, 759, L33
- Brodie, J. P., Romanowsky, A. J., Strader, J., et al. 2014, *ApJ*, 796, 52
- Bullock, J. S., Kravtsov, A. V., & Weinberg, D. H. 2001, *ApJ*, 548, 33
- Bullock, J. S., & Johnston, K. V. 2005, *ApJ*, 635, 931

- Caldwell, N., & Romanowsky, A. J. 2016, *ApJ*, 824, 42
- Carollo, C. M., de Zeeuw, P. T., & van der Marel, R. P. 1995, *MNRAS*, 276,
- Cooper, A. P., Cole, S., Frenk, C. S., et al. 2010, *MNRAS*, 406, 744
- Cooper, A. P., D'Souza, R., Kauffmann, G., et al. 2013, *MNRAS*, 434, 3348
- Cooper, A. P., Cole, S., Frenk, C. S., Le Bret, T., & Pontzen, A. 2017, *MNRAS*, 469, 1691
- Côté, P., Marzke, R. O., & West, M. J. 1998, *ApJ*, 501, 554
- Deason, A. J., Mao, Y.-Y., & Wechsler, R. H. 2016, *ApJ*, 821, 5
- Dekel, A., Stoehr, F., Mamon, G. A., et al. 2005, *Nat*, 437, 707
- Evans, N. W., An, J., & Walker, M. G. 2009, *MNRAS*, 393, L50
- Fakhouri, O., Ma, C.-P., & Boylan-Kolchin, M. 2010, *MNRAS*, 406, 2267
- Forbes, D. A., Brodie, J. P., & Grillmair, C. J. 1997, *AJ*, 113, 1652
- Forbes, D. A., Alabi, A., Romanowsky, A. J., et al. 2016, *MNRAS*, 458, L44
- Forbes, D. A., Alabi, A., Brodie, J. P., et al. 2017, *AJ*, 153, 114
- Forbes, D. A. 2017, *MNRAS*, 472, L104
- Forbes, D. A., Read, J. I., Gieles, M., & Collins, M. L. M. 2018, *MNRAS*,
- Forbes, D. A., Bastian, N., Gieles, M., et al. 2018, *Proceedings of the Royal Society of London Series A*, 474, 20170616
- Gao, L., Navarro, J. F., Cole, S., et al. 2008, *MNRAS*, 387, 536
- Garrison-Kimmel, S., Boylan-Kolchin, M., Bullock, J. S., & Lee, K. 2014, *MNRAS*, 438, 2578
- Garrison-Kimmel, S., Bullock, J. S., Boylan-Kolchin, M., & Bardwell, E. 2017, *MNRAS*, 464, 3108
- Georgiev, I. Y., Puzia, T. H., Goudfrooij, P., & Hilker, M. 2010, *MNRAS*, 406, 1967
- Gerhard, O. E. 1991, *MNRAS*, 250, 812
- Gerhard, O. E. 1993, *MNRAS*, 265, 213
- Gnedin, O. Y., & Ostriker, J. P. 1997, *ApJ*, 474, 223
- Gnedin, O. Y., Ostriker, J. P., & Tremaine, S. 2014, *ApJ*, 785, 71
- Grillmair, C. J., Freeman, K. C., Bicknell, G. V., et al. 1994, *ApJL*, 422, L9
- Grillmair, C. J., & Dionatos, O. 2006, *ApJL*, 643, L17
- Guo, Q., White, S., Li, C., & Boylan-Kolchin, M. 2010, *MNRAS*, 404, 1111
- Harris, W. E., Harris, G. L. H., & Alessi, M. 2013, *ApJ*, 772, 82
- Harris, W. E., Harris, G. L., & Hudson, M. J. 2015, *ApJ*, 806, 36
- Harris, W. E., Blakeslee, J. P., & Harris, G. L. H. 2017, *ApJ*, 836, 67
- Hudson, M. J., Harris, G. L., & Harris, W. E. 2014, *ApJL*, 787, L5
- Hudson, M. J., & Robison, B. 2017, *arXiv:1707.02609*
- Jethwa, P., Erkal, D., & Belokurov, V. 2018, *MNRAS*, 473, 2060
- Jiang, L., Cole, S., Sawala, T., & Frenk, C. S. 2015, *MNRAS*, 448, 1674
- Jordán, A., McLaughlin, D. E., Côté, P., et al. 2007, *ApJS*, 171, 101
- Kravtsov, A. V., & Gnedin, O. Y. 2005, *ApJ*, 623, 650
- Kruijssen, J. M. D., Pelupessy, F. I., Lamers, H. J. G. L. M., et al. 2012, *MNRAS*, 421, 1927
- Li, H., & Gnedin, O. Y. 2014, *ApJ*, 796, 10
- Ludlow, A. D., Navarro, J. F., Angulo, R. E., et al. 2014, *MNRAS*, 441, 378
- Mamon, G. A., Biviano, A., & Boué, G. 2013, *MNRAS*, 429, 3079
- Mieske, S., Küpper, A. H. W., & Brockamp, M. 2014, *AA*, 565, L6
- Mistani, P. A., Sales, L. V., Pillepich, A., et al. 2016, *MNRAS*, 455, 2323
- Moody, C. E., Romanowsky, A. J., Cox, T. J., Novak, G. S., & Primack, J. R. 2014, *MNRAS*, 444, 1475
- Moore, B., Diemand, J., Madau, P., Zemp, M., & Stadel, J. 2006, *MNRAS*, 368, 563
- Moster, B. P., Somerville, R. S., Maulbetsch, C., et al. 2010, *ApJ*, 710, 903
- Naab, T., Johansson, P. H., Ostriker, J. P., & Efstathiou, G. 2007, *ApJ*, 658, 710
- Napolitano, N. R., Pannella, M., Arnaboldi, M., et al. 2003, *ApJ*, 594, 172
- Napolitano, N. R., Pota, V., Romanowsky, A. J., et al. 2014, *MNRAS*, 439, 659
- Navarro, J. F., Frenk, C. S., & White, S. D. M. 1997, *ApJ*, 490, 493
- Odenkirchen, M., Grebel, E. K., Dehnen, W., et al. 2003, *AJ*, 126, 2385
- Oldham, L. J., & Auger, M. W. 2016, *MNRAS*, 457, 421
- Oñorbe, J., Domínguez-Tenreiro, R., Sáiz, A., & Serna, A. 2007, *MNRAS*, 376, 39
- Peebles, P. J. E. 1984, *ApJ*, 277, 470
- Peng, E. W., Jordán, A., Côté, P., et al. 2008, *ApJ*, 681, 197-224
- Pillepich, A., Vogelsberger, M., Deason, A., et al. 2014, *MNRAS*, 444, 237
- Pota, V., Forbes, D. A., Romanowsky, A. J., et al. 2013, *MNRAS*, 428, 389
- Pota, V., Romanowsky, A. J., Brodie, J. P., et al. 2015, *MNRAS*, 450, 3345
- Purcell, C. W., Bullock, J. S., & Zentner, A. R. 2007, *ApJ*, 666, 20
- Ramos-Almendares, F., Abadi, M. G., Muriel, H., & Coenda, V. 2017, *arXiv:1712.05410*
- Ricotti, M. 2002, *MNRAS*, 336, L33
- Rodríguez-Gomez, V., Pillepich, A., Sales, L. V., et al. 2016, *MNRAS*, 458, 2371
- Romanowsky, A. J., & Kochanek, C. S. 2001, *ApJ*, 553, 722
- Röttgers, B., Naab, T., & Oser, L. 2014, *MNRAS*, 445, 1065
- Saglia, R. P., Kronawitter, A., Gerhard, O., & Bender, R. 2000, *AJ*, 119, 153
- Sales, L. V., Navarro, J. F., Abadi, M. G., & Steinmetz, M. 2007, *MNRAS*, 379, 1464
- Schuberth, Y., Richtler, T., Hilker, M., et al. 2012, *AA*, 544, A115
- Spitler, L. R., & Forbes, D. A. 2009, *MNRAS*, 392, L1
- Strader, J., Romanowsky, A. J., Brodie, J. P., et al. 2011, *ApJS*, 197, 33
- van der Marel, R. P., & Franx, M. 1993, *ApJ*, 407, 525
- Vesperini, E., & Heggie, D. C. 1997, *MNRAS*, 289, 898
- Vesperini, E., Zepf, S. E., Kundu, A., & Ashman, K. M. 2003, *ApJ*, 593, 760
- Wasserman, A., Romanowsky, A. J., Brodie, J., et al. 2017, *arXiv:1712.01229*
- Wetzell, A. R. 2011, *MNRAS*, 412, 49
- White, S. D. M., & Frenk, C. S. 1991, *ApJ*, 379, 52
- Wu, X., Gerhard, O., Naab, T., et al. 2014, *MNRAS*, 438, 2701
- Zepf, S. E., & Ashman, K. M. 1993, *MNRAS*, 264, 611
- Zepf, S. E., Beasley, M. A., Bridges, T. J., et al. 2000, *AJ*, 120, 2928
- Zhang, H.-X., Peng, E. W., Côté, P., et al. 2015, *ApJ*, 802, 30
- Zhu, L., Long, R. J., Mao, S., et al. 2014, *ApJ*, 792, 59
- Zhu, L., Romanowsky, A. J., van de Ven, G., et al. 2016, *MNRAS*, 462, 4001
- Zonoozi, A. H., Rabiee, M., Haghi, H., & Küpper, A. H. W. 2016, *ApJ*, 818, 58